Petroleum Science 23 (2026) 3490–3505

Contents lists available at ScienceDirect

Petroleum Science

journal homepage: www.keaipublishing.com/en/journals/petroleum-science

Original Paper

Characteristics of fracturing fluid water blocking damage in tight gas reservoirs based on two-dimensional NMR T_1–T_2

Xiao-Hang Li [a,b,c], Hui Gao [a,b,c,*], Yong-Gang Xie [d,e], Hua-Qiang Shi [e], Hua-Zhou Li [f], Teng Li [a,b,c,g], Zhi-Lin Cheng [a,b,c], Chen Wang [a,b,c], Kai-Qing Luo [a,b,c]

[a] *College of Petroleum Engineering, Xi'an Shiyou University, Xi'an, 710065, Shaanxi, China*
[b] *Engineering Research Center of Development and Management for Low to Ultra-Low Permeability Oil & Gas Reservoirs in West China of Ministry of Education, Xi'an Shiyou University, Xi'an, 710065, Shaanxi, China*
[c] *Xi'an Key Laboratory of Tight Oil (Shale Oil) Development, Xi'an, 710065, Shaanxi, China*
[d] *Southern Sulige Operation Company, PetroChina Changqing Oilfield, Xi'an, 710018, Shaanxi, China*
[e] *National Engineering Laboratory for Exploration and Development of Low-Permeability Oil & Gas Fields, Xi'an, 710018, Shaanxi, China*
[f] *School of Mining and Petroleum Engineering, Faculty of Engineering, University of Alberta, Edmonton T6G 1H9, Canada*
[g] *State Key Laboratory of Oil and Gas Reservoir Geology and Exploration (Southwest Petroleum University), Chengdu, 610500, Sichuan, China*

A R T I C L E I N F O

Article history:
Received 17 September 2025
Received in revised form
9 March 2026
Accepted 10 March 2026
Available online 14 March 2026

Edited by Yan-Hua Sun

Keywords:
Tight gas reservoir
NMR T_1–T_2
Flowback of fracturing fluids
Retention of fracturing fluids
Degree of water blocking damage
Different pore scales

A B S T R A C T

In the development of tight gas reservoirs, effective flowback of fracturing fluids is crucial for enhancing production. However, water blocking damage caused by fluid retention significantly affects reservoir performance. This study utilizes nuclear magnetic resonance (NMR) T_2 and T_1–T_2 techniques to analyze water blocking damage during flowback, aiming to characterize fluid retention and the degree of water blocking damage. Reservoirs are classified into Type I, Type II, and Type III, based on the physical properties, pore-throat structure, and mineral composition of core. By integrating high-pressure mercury intrusion with NMR T_2 spectra, pores are categorized into macropores, mesopores, and micropores. The results indicate that micropores and mesopores are primary regions for fracturing fluid retention. As the flowback pressure differential increases, water blocking damage decreases, with Type I cores exhibiting lower water blocking damage compared to Type II and Type III cores. Furthermore, the integration of NMR T_2 and T_1–T_2 techniques enabled the establishment of distribution and occurrence charts of hydrogen-containing substances (hydrogen water, bound fluid, and free fluid) in three types of reservoirs. The T_1–T_2 spectra visualize pore development and fluid retention. During flowback, significant signal changes in bound water region indicate less retained fluid. The macropores have the lowest water blocking (<90%), while mesopores and micropores exceeds 90%. After flowback, mesopores exhibit most significant changes, while micropores have highest degree of water blocking damage, potentially resulting in long-term or permanent water blocking damage. This study investigates the mechanisms of fluid retention and water blocking across pore scales, providing a scientific basis for optimizing fracturing flowback.

1. Introduction

As global conventional oil and gas resources are depleting, tight oil and gas have become a focus of exploration and development (Zou et al., 2015, 2018). As an important unconventional resource, tight gas is crucial for future oil and gas production growth (Ma, 2021; Sun M.D. et al., 2019), particularly in achieving the “Double Carbon Target” (Ramalingam et al., 2020; Wang et al., 2019). However, the complex pore structure and heterogeneity of tight gas reservoirs present significant challenges for their development (Sun L.D. et al., 2019; Zhang Y.Y. et al., 2022). Compared to conventional natural gas reservoirs, tight gas reservoirs typically exhibit poor physical properties and great heterogeneity with storage spaces primarily consisting of secondary pores (Guo et al.,

* Corresponding author.
E-mail address: ghtopsun1@163.com (H. Gao).
Peer review under the responsibility of China University of Petroleum (Beijing).

https://doi.org/10.1016/j.petsci.2026.03.017
1995-8226/

2023; Zhao et al., 2021). Pore structures are frequently intricate, with limited pore connectivity (Liu et al., 2023; Zhou et al., 2022).

Fracturing has been demonstrated to be an effective technique for facilitating the development of tight gas reservoirs (Hu et al., 2018). However, the invasion of fracturing fluids into the reservoir matrix can lead to permeability damage, resulting in issues such as residual blocking, particle migration, clay mineral swelling, and liquid phase retention (Zhao et al., 2023), all of which reduce near-wellbore permeability and cause severe fracturing fluid damage (Tang et al., 2021). The most commonly observed forms of fracturing fluid damage are water sensitivity damage, water blocking damage, and solid phase retention of fracturing fluids (Almubarak et al., 2020). To mitigate the damage caused by fracturing fluids, timely flowback is essential (Wang et al., 2020a); otherwise, significant liquid phase retention can occur, forming a "liquid phase trap" and leading to water blocking (Xu et al., 2019). The fracturing fluid that is retained within the pores has the potential to invade the reservoir further (Wang et al., 2020b), thereby altering the ratio of bound to free fluids. This results in an increase in the bound fluid content and a concomitant decrease in fluid mobility (Fu et al., 2020). The strong capillary pressure in water-wet formations, caused by small pore throats and poor connectivity, results in the accumulation of fracturing fluid on the rock surface and within the throats, which in turn impedes the flowback process (Naik et al., 2019). Capillary forces and the Jamin effect facilitate the intrusion of external fluids (Huang et al., 2020), resulting in water blocking damage and reducing production from tight gas reservoirs (Bahrami et al., 2015).

The characteristics of reservoir fracturing fluid damage are largely determined by pore structure. Accurately characterizing this structure and employing complementary techniques are essential for effectively preventing damage from fracturing fluids. Zhang X.P. et al. (2023) successfully identified pore structure features using fractal dimension (D_2) and mercury intrusion parameters; however, their method does not adequately reflect the microstructure and dynamic behavior of pores during fluid flow. Wang and Zhou (2021) employed scanning electron microscopy (SEM) to analyze core microstructure before and after exposure to fracturing fluid, clarifying the damage mechanisms; however, their study lacked a systematic examination of pore structure evolution. Li et al. (2019) utilized micro-CT to obtain three-dimensional images of the reservoir geometry to assess fracturing fluid damage, but this approach has high sample preparation demands and resolution limitations, making it challenging to capture subtle changes. Zhang X.P. et al. (2022) analyzed mineral composition and expansion characteristics using X-ray diffraction (XRD) and dilatometry, but this method focuses too much on mineral components, neglecting pore structure and fluid interactions. Tang et al. (2021) conducted core flooding experiments and reported that water-based fracturing fluids caused a 40%–60% reduction in the permeability of tight sandstones, indicating moderate to severe water blocking damage. Guo et al. (2024) performed gas displacement tests on nine tight sandstone cores and found that low-permeability reservoirs exhibited more pronounced water blocking based on permeability recovery ratios. Song et al. (2024) used micro-CT to reconstruct the pore network of ultra-tight sandstones from the Tarim Basin and revealed that water blocking damage was mainly concentrated in micropores of 0.01–0.1 μm, where pore connectivity decreased by more than 50%.

Tight gas reservoirs are characterized by complex pore structures, strong heterogeneity, and diverse fluid distribution states, making it challenging for conventional methods to accurately characterize reservoir parameters and fluid behavior. Nuclear magnetic resonance (NMR) technology, with its advantages of non-destructive measurement, continuous monitoring, and multi-parameter response, has become a core tool for studying tight gas reservoirs (Wang et al., 2023). Wu et al. (2020) calculated the fractal dimension of tight sandstone reservoirs directly from NMR echo data, overcoming the limitations of traditional methods that rely solely on T_2 distributions. While Li Y.Z. et al. (2022) employed NMR T_2 experiments to quantify porosity damage, their analysis primarily addressed T_2 spectral properties without adequately considering fluid dynamics. Gu et al. (2023) proposed a two-dimensional (2D) NMR fluid saturation evaluation method combining morphological analysis, non-negative matrix factorization, and fully constrained least squares. This method uses the Akaike information criterion (AIC) to automatically determine the number of fluid types in tight reservoirs, including free water, bound water, and light hydrocarbons. To address the high uncertainty in conventional fluid identification in tight sandstone gas reservoirs, Li et al. (2025) developed a dual-algorithm inversion method based on particle swarm optimization (PSO) and least squares (LSQR) using NMR dual-echo time (TE) logging data. This approach improved gas layer identification accuracy from 65% to 92%. He Y.W. et al. (2024) applied online NMR monitoring to continuously track fluid migration at various pore scales during depleted development of tight reservoirs. Using dual-peak features of T_2 spectra, they accurately identified pore distributions dominated by micron-nanometer scale pore throats (<0.1 μm), confirming that fluid retention in micropores is the primary factor limiting recovery. Most existing studies rely on one-dimensional (1D) NMR T_2 spectra, which can only distinguish between "free fluid" and "bound fluid" and cannot identify specific fluid types such as hydrogen water. This leads to ambiguous differentiation between fracturing fluid and formation water, resulting in significant errors in water blocking damage quantification. Additionally, the T_2 relaxation time and pore radius conversion coefficient (C) is typically set empirically, leading to inaccurate pore classification and preventing clear assessment of the contributions of different pore scales to water blocking damage. Furthermore, existing experiments lack dynamic data under varying flowback pressure differentials, making it impossible to capture the continuous process in which an increasing pressure differential leads to fluid displacement and subsequent mitigation of water blocking damage, leaving the dynamic regulation mechanism of water blocking damage without experimental support.

Considering the characteristics of tight gas reservoirs, including low porosity, low permeability, and well-developed small pore throats, this study integrates one-dimensional (1D) NMR T_2 spectra and two-dimensional (2D) NMR T_1–T_2 spectra to develop a multi-scale pore-fluid characterization method. The 1D T_2 spectra are employed to classify pores into macropores, mesopores, and micropores and to preliminarily quantify water blocking damage, while the 2D T_1–T_2 spectra enable precise identification of hydrogen-containing substances, including hydrogen water, bound fluid, and free fluid, these results establish the distribution and occurrence charts of hydrogen-bearing substances and enable a comprehensive analysis of pore characteristics, fluid occurrence, and water blocking damage. This methodology allows quantitative assessment of water blocking damage across different pore scales, accurately identifies the primary pore domains responsible for water blocking, and establishes the quantitative relationships among flowback pressure, pore scale, and fluid retention, and elucidates the underlying coupled mechanisms. These findings provide a theoretical foundation for understanding water blocking damage and are essential for the optimal development of tight gas resources.

2. Theoretical background

2.1. Nuclear magnetic resonance principle

NMR involves the interaction between an external magnetic field and the spin angular momentum of hydrogen in core samples

(Li T. et al., 2022). The T_2 relaxation times of fluids in the pores can be expressed as follows:

$$\frac{1}{T_2} = \frac{1}{T_{2B}} + \frac{1}{T_{2S}} + \frac{1}{T_{2D}} \tag{1}$$

where T_2 is the transverse relaxation time, ms; T_{2B} is the bulk transverse relaxation time, ms; T_{2S} is the transverse surface relaxation time, ms; T_{2D} is the diffusion relaxation time, ms.

The T_2 relaxation time of fluids is primarily composed of surface and bulk relaxations. The relationship between specific surface area and pore radius (r) is expressed by the following formula:

$$S/V = F_S/r$$

where F_S is a dimensionless pore shape factor that varies with pore-throat size (Dai et al., 2019; Gao et al., 2024). Therefore, T_{2S} can be expressed as follows:

$$T_{2S} = \frac{1}{\rho_2 F_S} r \tag{2}$$

Let

$$\rho_2 F_S = C\rho_2$$

where ρ_2 is the surface relaxivity, μm/ms.

Neglecting the bulk relaxation T_{2B}, Eq. (2) can be expressed as follows:

$$r = CT_2 \tag{3}$$

where C is a dimensionless proportional constant.

2.2. Pore-radius conversion method

Taking the logarithm of both sides of Eq. (3) yields Eq. (4). By integrating the pore-throat size distribution obtained from mercury intrusion with the NMR data, the conversion coefficient C in Eq. (3) can be determined, thereby enabling the calculation of pore radius from the converted T_2 values (Gao et al., 2023).

$$\log(r) = \log(C) + \log(T_2) \tag{4}$$

Using Eq. (5), the deviation (δ) between the pore-throat radius calculated from the NMR T_2 spectrum and those obtained from mercury intrusion is evaluated. The optimal value of C is identified when the deviation δ reaches its minimum, and this optimal C is then used to derive the pore-throat size distribution converted from T_2.

$$\delta = \frac{\sqrt{\sum_{i=1}^{n}[r_i - (CT_{2i})]^2}}{100} \tag{5}$$

2.3. Calculation of water blocking degree

The objective is to calculate the area ratios of the NMR T_2 spectra curves for a range of core types to quantitatively evaluate the retention patterns of fracturing fluids within the pores and assess the degree of water blocking damage. The NMR curves for the initial water blocking state of the fracturing fluid (represented by the red curve) and for varying flowback pressure differential conditions (represented by the blue curve) (Fig. 1). The proportions of different pore scales are represented as S_{total}, S_{micro}, S_{meso}, and S_{macro}, respectively.

$$S_{\text{total}} = \frac{B_1 + B_2 + B_3}{A_1 + A_2 + A_3 + B_1 + B_2 + B_3} \times 100\% \tag{6}$$

$$\begin{cases} S_{\text{micro}} = \dfrac{B_1}{A_1 + B_1} \times 100\% \\ S_{\text{meso}} = \dfrac{B_2}{A_2 + B_2} \times 100\% \\ S_{\text{macro}} = \dfrac{B_3}{A_3 + B_3} \times 100\% \end{cases} \tag{7}$$

where S_{total}, S_{micro}, S_{meso}, and S_{macro} represent the retention rates of fracturing fluids in total pores, micropores, mesopores, and macropores, respectively, which indicate the degree of water blocking; A_1, A_2, and A_3 represent the differences in T_2 spectrum areas for micropores, mesopores, and macropores, respectively, between the initial water blocking state and the conditions under different flowback pressure differentials; B_1, B_2, and B_3 represent the T_2 spectrum areas for micropores, mesopores, and macropores under the various flowback pressure differential conditions.

To further elucidate the characteristics of fluid distribution and occurrence and to distinguish the signal values of different fluids (Zhang P.F. et al., 2023), a two-dimensional (2D) NMR T_1–T_2 scan is conducted using the Saturation-Recovery-Carr-Purcell-Meiboom-Gill (SR-CPMG) sequence to obtain comprehensive transverse and longitudinal relaxation signals. In 2D NMR experiment, the data obtained typically forms a two-dimensional matrix, $M(t_1, t_2)$, representing the signal intensity at time points t_1 and t_2. The 2D Laplace transformation and associated numerical methods are employed to derive the 2D T_1–T_2 spectral distribution, which offers a representation of fluid distribution within the rock (Li C.L. et al., 2022; Montrazi et al., 2018).

3. Experimental

3.1. Experimental materials

The samples utilized in this experiment were collected from the Shan 1 member of the Sulige Gas Field, located in the Ordos Basin. The physical properties, pore-throat structures, and mineral compositions of 50 samples from the study area were analyzed, and three different reservoir types were subsequently classified

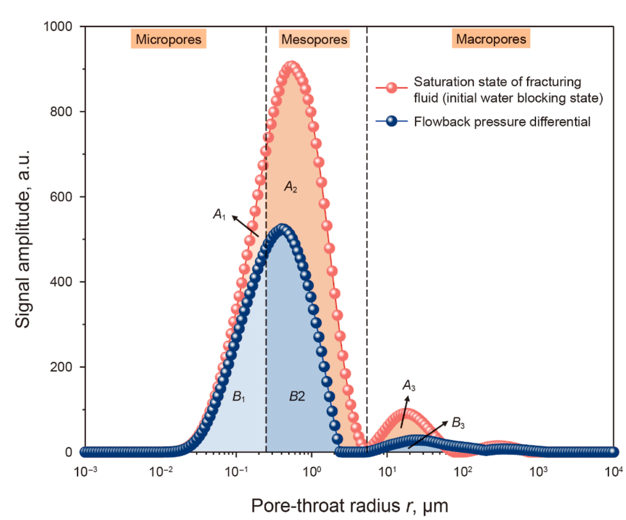

Fig. 1. Calculation of the degree of water blocking of fracturing fluid at different pore scales.

(Table 1). The rock type is lithic sandstone, with pore types mainly consisting of intergranular pores and dissolution pores (Fig. 2). The mineral composition is predominantly quartz, with the clay minerals are mainly kaolinite and illite (Fig. 3). The mercury intrusion curves of Type I and Type II reservoirs exhibit distinct platform stages, characterized by low displacement pressure, large median radius, high mercury saturation, and low saturation median pressure. In contrast, Type III reservoirs are characterized by high displacement pressure, small median radius, low mercury saturation, and high saturation median pressure, indicating progressively improving pore-throat interconnectivity from Type III to Type I reservoirs (Fig. 4).

Following the reservoir classification, cores representative of each of the three types of reservoirs were selected for experimentation. The simulated formation water, prepared according to the composition of the formation water from the Shan 1 member, is of the $CaCl_2$ type, with a salinity of 27,200 mg/L. The fracturing fluid system employed is a guar gum fracturing fluid with a pH range of 7–10. Detailed information on the cores used in the experiments is provided in Table 2.

3.2. Experimental equipment and parameters

The main experimental equipment (Fig. 5) included an NMR spectrometer, a displacement pump, an intermediate container, a core holder, a confining/back pressure pump, and pressure gauges. The 2PB constant flow pump is manufactured by Beijing Xingda Technology Development Co., Ltd. The core analysis was performed using a PQ001 NMR analyzer (Suzhou Niumag Analytical Instrument Co., Ltd.), which operated at a magnetic field intensity of 0.28±0.03 T and a pulse frequency of 1–30 MHz, with a control accuracy of 0.1 Hz. The instrument was equipped with a 25 mm diameter probe, making it suitable for samples longer than 25 mm.

The parameters for NMR experiments were as follows: the magnet was operated at a constant temperature of 32 °C. The CPMG and SR-CPMG sequences were used to measure T_2 and T_1–T_2 spectra, respectively. For the CPMG sequence, the parameters were as follows: a repeat sampling wait time of 2500 ms, an echo time of 0.10 ms, 5000 echoes (NECH), and 64 scans. For SR-CPMG sequence, the parameters were set as follows: a wait time of 10 ms, an echo time of 0.10 ms, 5000 echoes, and 32 scans. A short wait time was chosen to shorten acquisition time. To avoid misinterpretation of fluid signals due to differences in relaxation times, 25 inversion times were used, with inversion time of 2500 ms to ensure complete relaxation recovery of the sample. The measurement temperature was 32 °C (±0.5 °C). Samples were measured either in a state of fully saturated with simulated formation water or after displacement under different flowback pressure differential conditions.

3.3. Experimental procedure

1) The core sample was dried in an incubator for 24 h, followed by gas permeability measurement (gas permeability). The sample was evacuated and then saturated with formation water for 24 h to measure porosity.
2) N_2 was injected at a pressure of 0.5 MPa until no further liquid was produced at the outlet, establishing the initial gas–water distribution state.
3) Under the simulated formation temperature (80 °C), the fracturing fluid was injected in the reverse direction at a rate of 0.05 mL/min until 10 pore volumes (PV) of fracturing fluid were injected. The inlet and outlet ends were then closed and the sample was allowed to soak for 12 h.
4) The N_2 flowback pressure differential is set to 2 MPa. Gas injection was continued until no liquid was produced at the outlet, after which NMR testing was performed.
5) The core type and flowback pressure differential were varied, with pressures set to 4, 6, and 8 MPa. Steps 1) through 4) were repeated for each condition.
6) NMR T_2 and T_1–T_2 spectra were used to determine fluid distribution and quantify the degree of water blocking. The characteristics of water blocking induced by fracturing fluid were analyzed, and the underlying water blocking damage mechanisms were elucidated.

4. Results and discussion

4.1. Characteristics of NMR T_2 spectrum changes

4.1.1. Pore transformation and classification

The transverse relaxation time T_2 obtained from NMR reflects the size of the pore space in rocks and is positively correlated with the pore-throat radius (Gao et al., 2015). By integrating the mercury intrusion results with the pore-throat distribution of the Type I reservoir cores, the conversion coefficient C in Eq. (3) can be determined, thereby enabling the transformation of T_2 into the corresponding pore radius (Gao et al., 2023). Due to differences in the number of sampling points and interval densities between the two experiments, the original cumulative curves cannot be directly matched. Therefore, interpolation is required to align the data. Using the pore-throat radius converted from the NMR T_2 spectrum as a reference, the cumulative pore volumes from the mercury intrusion curve are linearly interpolated. The deviation between the interpolated mercury intrusion and NMR cumulative pore volumes is calculated to ensure the reliability of the interpolation.

Based on Eq. (4), the relative cumulative distribution curve of pore-throat radius obtained from mercury intrusion can be plotted against $\log(r)$. Different C values were selected to calculate the relative cumulative distribution curves of $\log C + \log T_2$ (Fig. 6). Additionally, using Eq. (5), the deviation (δ) between the pore-throat converted from T_2 spectra and those obtained from mercury intrusion tests was computed. When the δ reaches a minimum, the C value is considered optimal (Fig. 7), and the T_2-derived pore-throat size distribution is obtained (Fig. 8). The aforementioned approach was employed to determine the optimal C values for reservoir cores of Type II and Type III classifications, allowing for the conversion of T_2 values to pore-throat radius (Table 3). The calculated fitting accuracies (R^2) are 0.952, 0.934, and 0.947, respectively.

Table 1
Classification of different types of reservoirs.

Reservoir type	Permeability, 10^{-3} μm^2	Porosity, %	Displacement pressure, MPa	Median radius, μm	Maximum mercury saturation, %	Saturation median pressure, MPa
Type I	≥0.5	≥5	0.138	0.564	90.872	1.303
Type II	<0.5	≥5	0.675	0.044	83.963	16.600
Type III	<0.5	<5	2.747	0.006	59.861	118.350

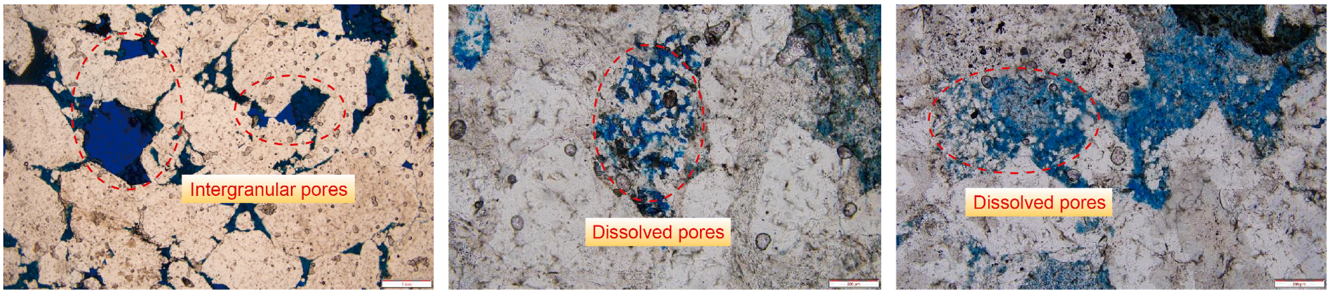

Fig. 2. Pore types of core samples.

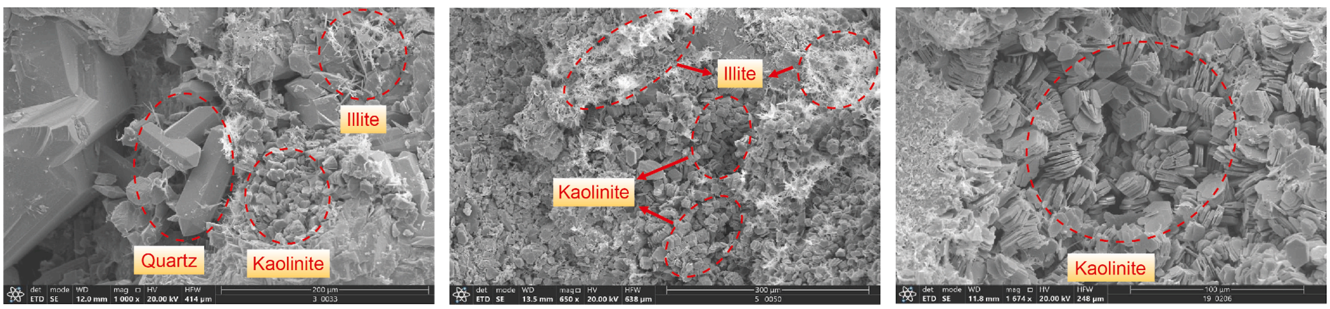

Fig. 3. Mineral composition of core samples.

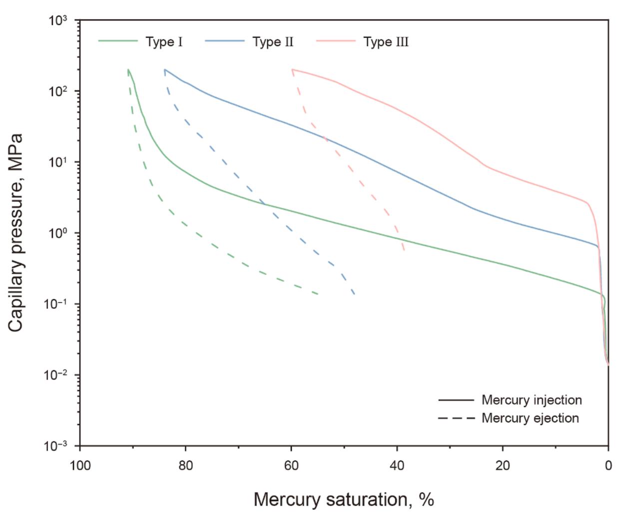

Fig. 4. High-pressure mercury injection and ejection curves for core samples.

To investigate the degree of water blocking damage at different pore scales, the T_2 distribution characteristics of the three types of cores saturated with formation water are subjected to analysis. By integrating the pore-throat radius distribution obtained from mercury intrusion tests with the NMR pore conversion results, the pores in the cores were classified by radius size. This classification corresponds to T_2 as follows: micropores (T_2 < 0.25 ms), mesopores (0.25 ms $\leq T_2 <$ 5.41 ms), and macropores ($T_2 \geq$ 5.41 ms). Using the conversion coefficient C, T_2 was converted into pore-throat radius (r). Applying this classification to the NMR T_2 spectra enables further analysis of the damage extent at different pore scales.

4.1.2. Variation features of T_2 spectra and pore distribution

The T_2 spectrum test results of cores from different reservoir types under different flowback pressure differentials reveal a bimodal distribution, characterized by a higher left peak amplitude and a lower right peak (Fig. 9). Type I cores exhibit a well-developed macropores, while Type II and Type III cores have a generally moderate development of macropores. At the initial state (0 MPa), the left-peak amplitude of the Type I core is 7446.67 a.u. (a.u., arbitrary units of signal intensity), and the right-peak amplitude is 7684.73 a.u. For the Type II core, the left-peak and right-peak amplitudes are 10767.02 and 3147.81 a.u., respectively. For the Type III core, the corresponding values are 10349.15 and 2097.31 a.u. These results indicate that mesopores and micropores constitute the primary fluid retention spaces in all three reservoir types, and the amplitude difference between the left and right peaks becomes increasingly pronounced as reservoir quality deteriorates from Type I to Type III.

As the flowback pressure differential increases, the NMR curves for all three types of cores shift leftward, and the amplitude decreases. The retention of fracturing fluid in mesopores and macropores significantly decreases. This demonstrates that increasing the flowback pressure differential can effectively reduce water

Table 2
Information of experimental core samples.

Core type	Permeability, 10^{-3} μm^2	Porosity, %	Fracturing fluid	Reservoir type
Type I core	0.5750	5.86	Guar gum fracturing fluid	Type I
Type II core	0.3521	5.52		Type II
Type III core	0.3389	2.94		Type III

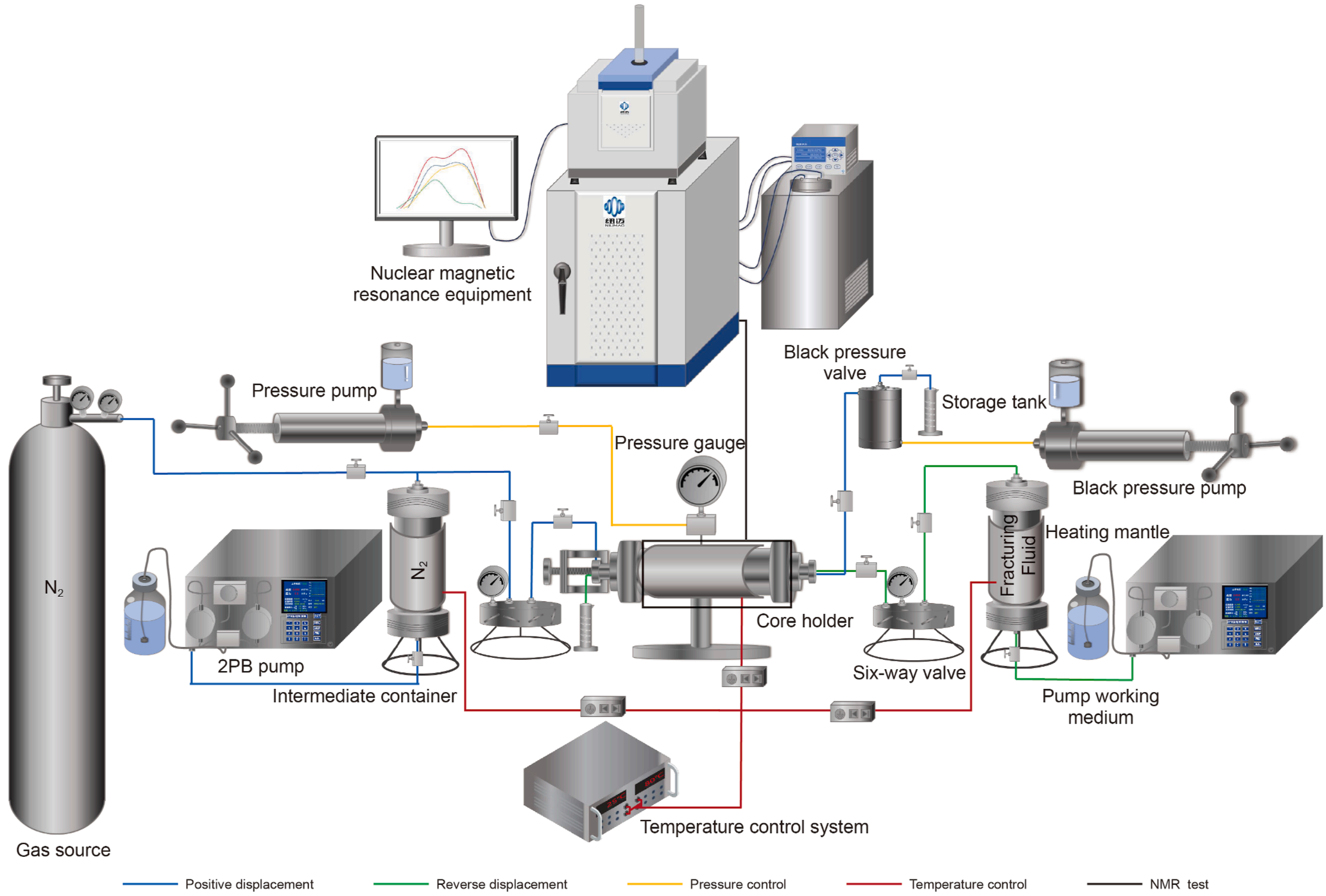

Fig. 5. Experimental equipment.

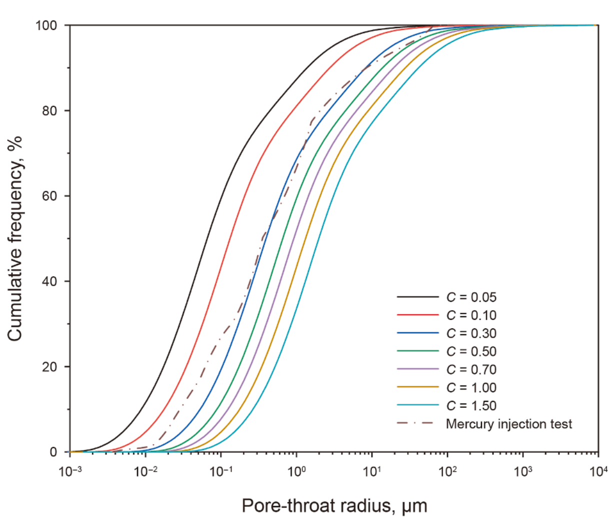

Fig. 6. Impact of conversion coefficient C on the cumulative frequency of pore-throat radius.

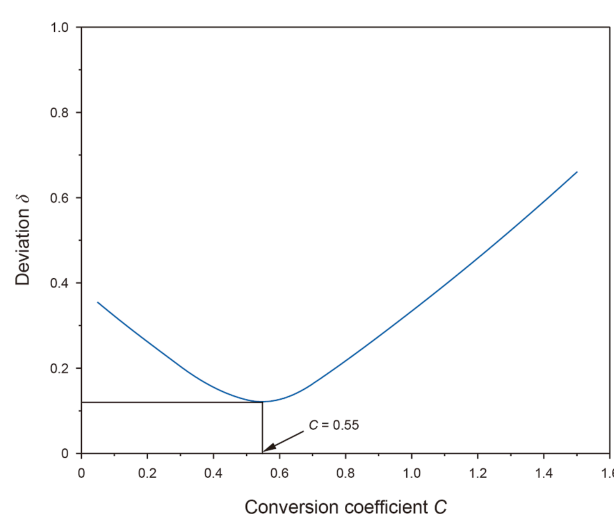

Fig. 7. Deviation between measured and calculated cumulative frequency of pore-throat radius at different C.

blocking damage in macropores and mesopores. However, the fracturing fluid retained in micropores remains difficult to flow-back, which results in greater water blocking damage. Following the completion of flowback, Type I cores exhibit the lowest amplitude in the curves and the least fluid retention, with the water blocking damage significantly lower than that observed in Type II and Type III cores.

The NMR T_2 spectrum results (Fig. 10) indicate that the primary peak of NMR curves for Type I cores is distributed between 0.25 and 5.41 μm, indicating that mesopores serve as the primary retention space for fracturing fluids. The primary peaks are distributed between 0.11 and 1.87 μm for Type II cores and between 0.06 an 1.24 μm for Type III cores, respectively. This indicates that both micropores and mesopores are primary retention

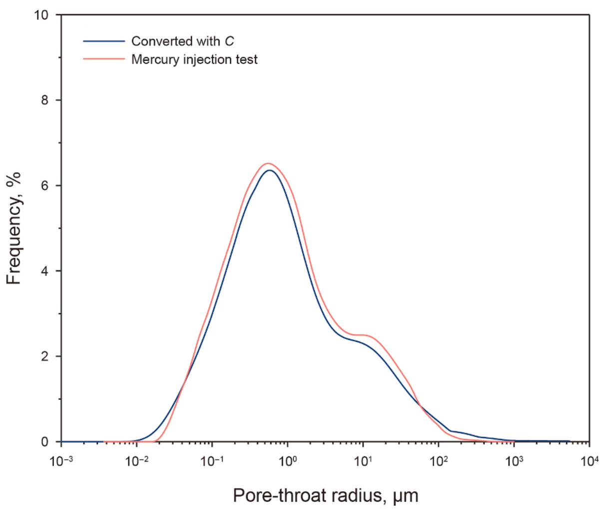

Fig. 8. Pore-throat size distribution derived from mercury intrusion testing and transformed from NMR T_2 measurements.

Table 3
Pore conversion coefficients for three types of reservoir cores.

Reservoir type	Conversion coefficient C	R^2
Type I	0.55	0.952
Type II	1.47	0.934
Type III	3.09	0.947

spaces for fracturing fluids in Type II and III cores. As the N_2 flowback pressure differential increases, the primary peaks of the curves for all three core types shift significantly leftward, indicating a transition of the main retention region from mesopores to micropores. Upon completion of the flowback process, micropores become the primary region for fracturing fluid retention. In Type I and Type II cores, the water blocking region shifts from mesopores to micropores. In Type III cores, however, the water blocking region remains predominantly in micropores.

The variation in the NMR T_2 spectrum area can further reflect the development characteristics of the pore structure and the retention degree of fracturing fluid (Fig. 11). Prior to fracturing fluid flowback, the NMR signal areas of macropores and mesopores in Type I reservoirs are significantly higher than those in Type II and Type III reservoirs, indicating a more developed pore structure in Type I reservoir cores. Among the three types of reservoir types, mesopores exhibit the largest NMR signal area, followed by micropores, suggesting that fracturing fluid is predominantly retained in mesopores and micropores. The NMR signal area of micropores shows relatively minor changes, with only a slight decrease as the flowback pressure differential increases, indicating substantial retention of fracturing fluid in micropores. The variation in the NMR signal area of mesopores is comparatively larger across the three reservoir types, highlighting mesopores as the primary retention space for fracturing fluid and a key factor influencing the total pore NMR signal area. As the main flow channels, the NMR signal area of macropores also decreases with increasing flowback pressure differential, reflecting the extent of fracturing fluid retention in macropores. Moreover, the NMR T_2 spectrum area can be further used for the quantitative evaluation of water blocking damage.

4.2. T_1–T_2 spectrum characteristics of fluid occurrence

4.2.1. 2D NMR T_1–T_2 maps of fluid occurrence

In core samples saturated with hydrogen-containing fluids, the diffusion-coupling effect causes random molecular diffusion between different pores. This diffusion results in overlapping relaxation signals of different fluids in the one-dimensional NMR T_2 spectrum, making it difficult to distinguish the hydrogen-containing substances within the pores. The two-dimensional NMR T_1–T_2 spectrum can effectively resolve these overlapping hydrogen signals (Li et al., 2024; Silletta et al., 2022).

The 2D NMR T_1–T_2 spectroscopy can effectively distinguish the overlapping hydrogen signals. The boundary values for different types of hydrogen-containing substances are determined based on the T_2 spectra of the cores in different states. In the T_1–T_2 spectrum, the regions in which various hydrogen-bearing substances are distributed are delineated, thereby establishing distribution charts for hydrogen-containing substances in different types of reservoirs (He J.W. et al., 2024). The T_2 spectra of the dry, water saturated, and centrifuged states of the three types of reservoir cores are obtained through measurement. According to the method proposed by Gao and Li (2015), the T_2 spectra of cores in different states were aggregated to obtain the cumulative distribution curves for each reservoir type (Fig. 12). The cumulative distribution curves are then extended backward in order to ascertain the boundary values, which can be identified as the intersection points between these curves and the NMR T_2 spectrum curves. The boundary values for hydrogen water and bound fluid for the three types of reservoirs are 0.2796, 0.1500, and 0.1874 ms, respectively. The boundary values between bound and free fluids are 11.7538, 5.2396, and 10.4505 ms, respectively.

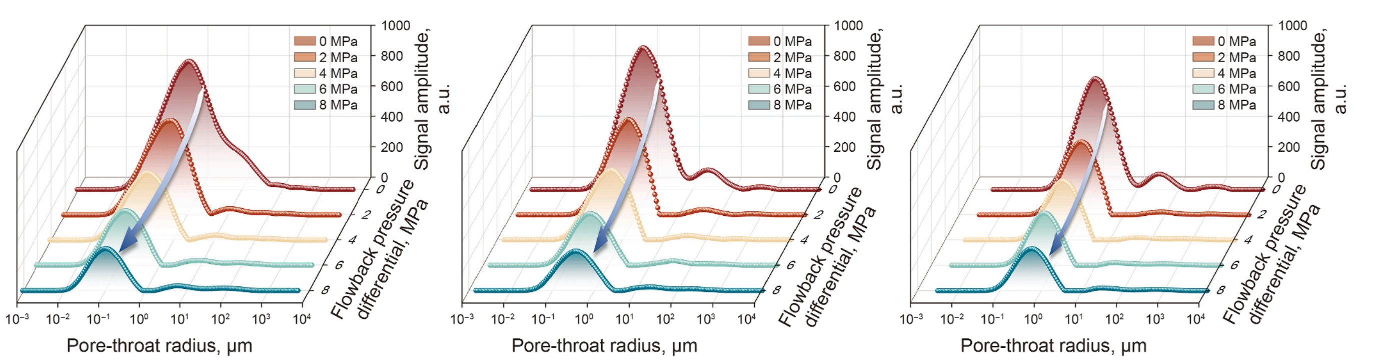

Fig. 9. NMR T_2 spectra and pore distribution of three types of reservoir cores.

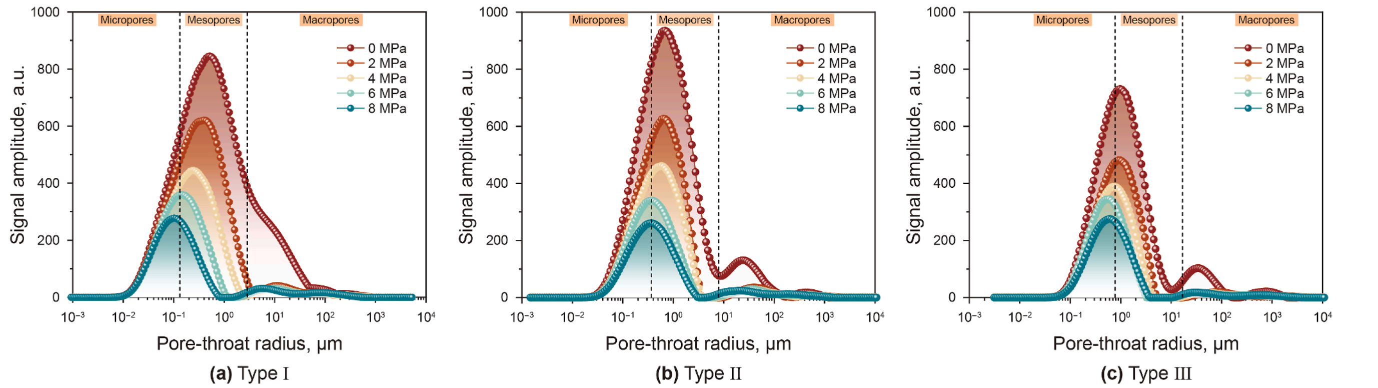

Fig. 10. T_2 distribution characteristics across different pore scales for three types of reservoir cores.

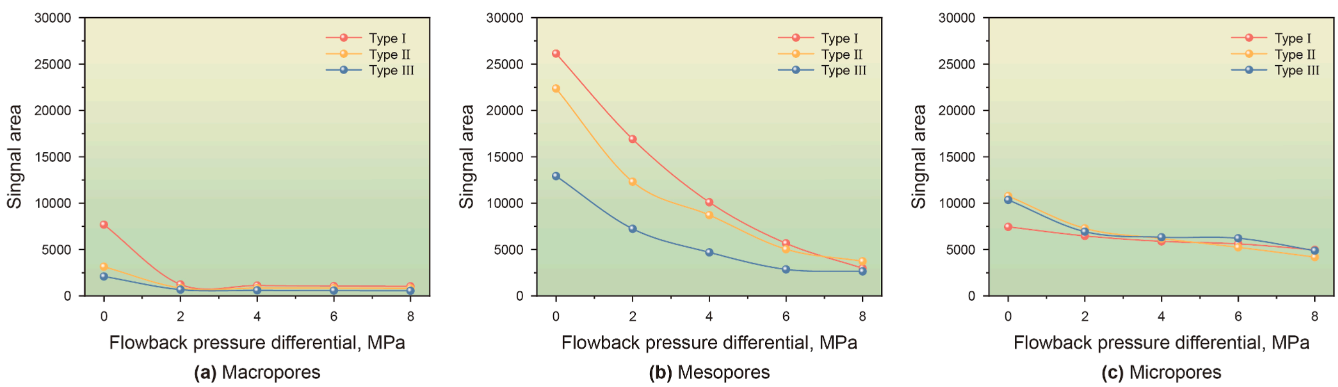

Fig. 11. Variation of NMR T_2 spectrum area for different pore scales.

By integrating the boundary values with the NMR T_1–T_2 spectrum (Fig. 13), the sources of hydrogen signals can be classified into three regions: the free fluid region, the bound fluid region, and the hydrogen water region. These are subsequently designated as region i, region ii, and region iii, respectively. The objective is to establish distribution maps for different hydrogen-containing substances (Fig. 14).

Region i: The hydrogen signals primarily originate from hydrogen water, such as the water found in the interlayer structure of clay. In comparison to free water, the hydrogen index of hydrogen water is markedly lower and can be disregarded in water-saturated samples.

Region ii: The hydrogen signals in this region mainly come from bound fluid in the pores, which exists in a thin film on the surfaces of rock particles or in small pores. This bound fluid exhibits low mobility and will not be transported from the formation by fluid flow.

Region iii: This region is primarily identified as containing movable water in the pores, which typically resides in larger pores and fractures. The bond between this water and the rock particles is comparatively weaker, which allows for free movement.

Fluid types within the pores were identified using T_1–T_2 spectra acquired via the SR-CPMG sequence. By using the differences in T_1 and T_2 values of different fluids, the pore size intervals defined by the T_2 spectrum were further refined to establish a correspondence between pore scale and fluid type, as summarized in Table 4.

4.2.2. Characteristics of T_1–T_2 spectrum variations

In the T_1–T_2 spectrum, darker colors represent higher signal intensity, which corresponds to greater fluid saturation (Singer

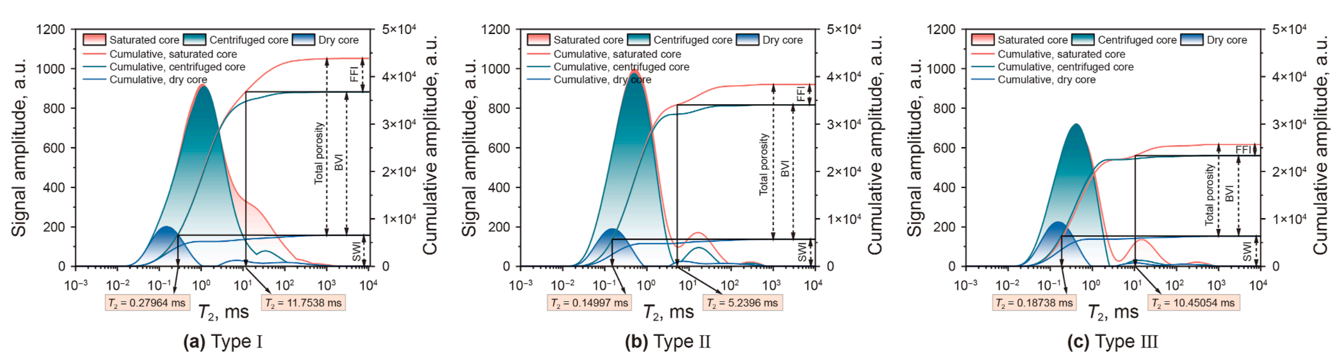

Fig. 12. T_2 spectrum characteristics of hydrogen-containing substances in different types of reservoirs.

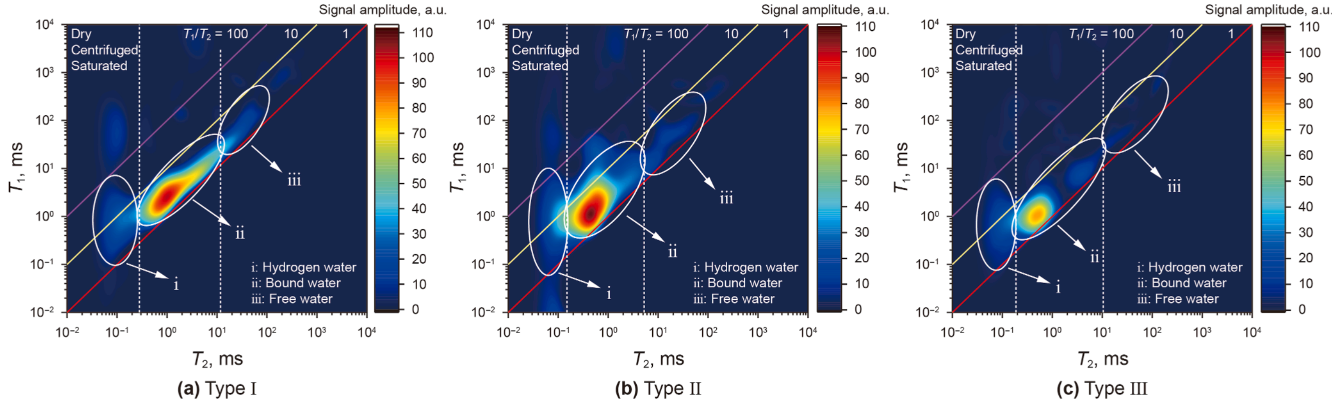

Fig. 13. Classification of hydrogen-containing substances in 2D NMR T_1–T_2 spectra.

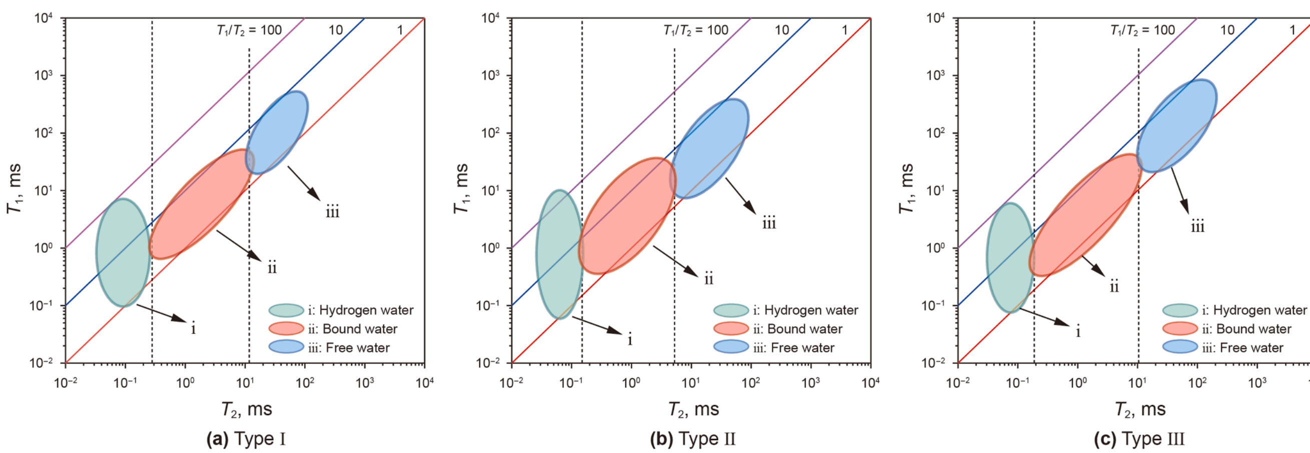

Fig. 14. 2D NMR T_1–T_2 map showing the distribution of hydrogen-containing substances.

et al., 2020). In accordance with the established distribution maps, the compactness and continuity of the various regions reflect the development degree of the different pore types. In Type I cores (Fig. 15(a1)), regions i, ii, and iii exhibit good continuity, with signal values distributed within $T_1/T_2 = 1$–10, indicating well-developed pores. For Type II cores (Fig. 15(b1)), the signal values range from $T_1/T_2 = 1$ to 100, indicating a more complex pore structure. In contrast, the three regions in Type III cores (Fig. 15(c1)) appear relatively isolated, with signal values also falling within $T_1/T_2 = 1$–10, indicating a less developed pore structure.

At a flowback pressure differential of 2 MPa (Fig. 15(a2)), the signal value in region iii disappears, indicating that the fracturing fluid in the macropores has been nearly completely flowback. The primary peak can be identified at $T_1 = 2.3025$ ms and $T_2 = 0.6959$ ms, with a signal value of 42.3072 a.u. The reduction in the signal area of region ii indicates a decrease in the amount of fracturing fluid retained in the pores, which reduces water blocking damage. Upon reaching a pressure differential of 6 MPa (Fig. 15(a4)), the signal value in region ii shifts leftward, while the fluid within macropores and mesopores experiences a marked decrease. In the subsequent phase of flowback (Fig. 15(a5)), regions i and ii become the primary site for fracturing fluid retention. The primary peak is situated at $T_1 = 0.4039$ ms and $T_2 = 0.1095$ ms, with a signal value of 16.3595 a.u., indicative a heightened degree of water blocking damage in the micropores.

Type II and Type III cores have analogous patterns to those observed in Type I cores. As the flowback pressure differential increases, the signal values in regions ii and iii change more slowly, and their areas decrease, ultimately concentrating within the range of $T_1/T_2 = 1$–10. In Type II cores, the signal value in region iii is essentially absent, indicating a considerable diminution in water blocking damage. The primary peak shifts to $T_1 = 0.9644$ ms and $T_2 = 0.2103$ ms, with the signal value decreasing from 26.6261 to 12.4278 a.u. (Fig. 15(b5)). In Type III cores, the signal alterations in region ii are the most notable, with the primary peak shifting to $T_1 = 0.5598$ ms and $T_2 = 0.2103$ ms, while the signal value decreases from 32.1595 to 8.8723 a.u. (Fig. 15(c5)).

The degree of fracturing fluid retention was quantitatively evaluated by calculating the area variations of different T_1–T_2 spectral regions in Fig. 15, with the results shown in Fig. 16. As the

Table 4
Correspondence between fluid type and pore scale.

Pore size interval in T_2 spectrum, ms	Corresponding pore type	T_1–T_2 spectrum region	Fluid type	Contribution to water blocking damage
$T_2 < 0.25$	Micropores	Region i	Hydrogen water	Core contributor to permanent water blocking
$0.25 \le T_2 < 5.41$	Mesopores	Region ii	Bound fluids	Major contributor to water blocking
$T_2 \ge 5.41$	Macropores	Region iii	Free fluids	Water blocking easily alleviated

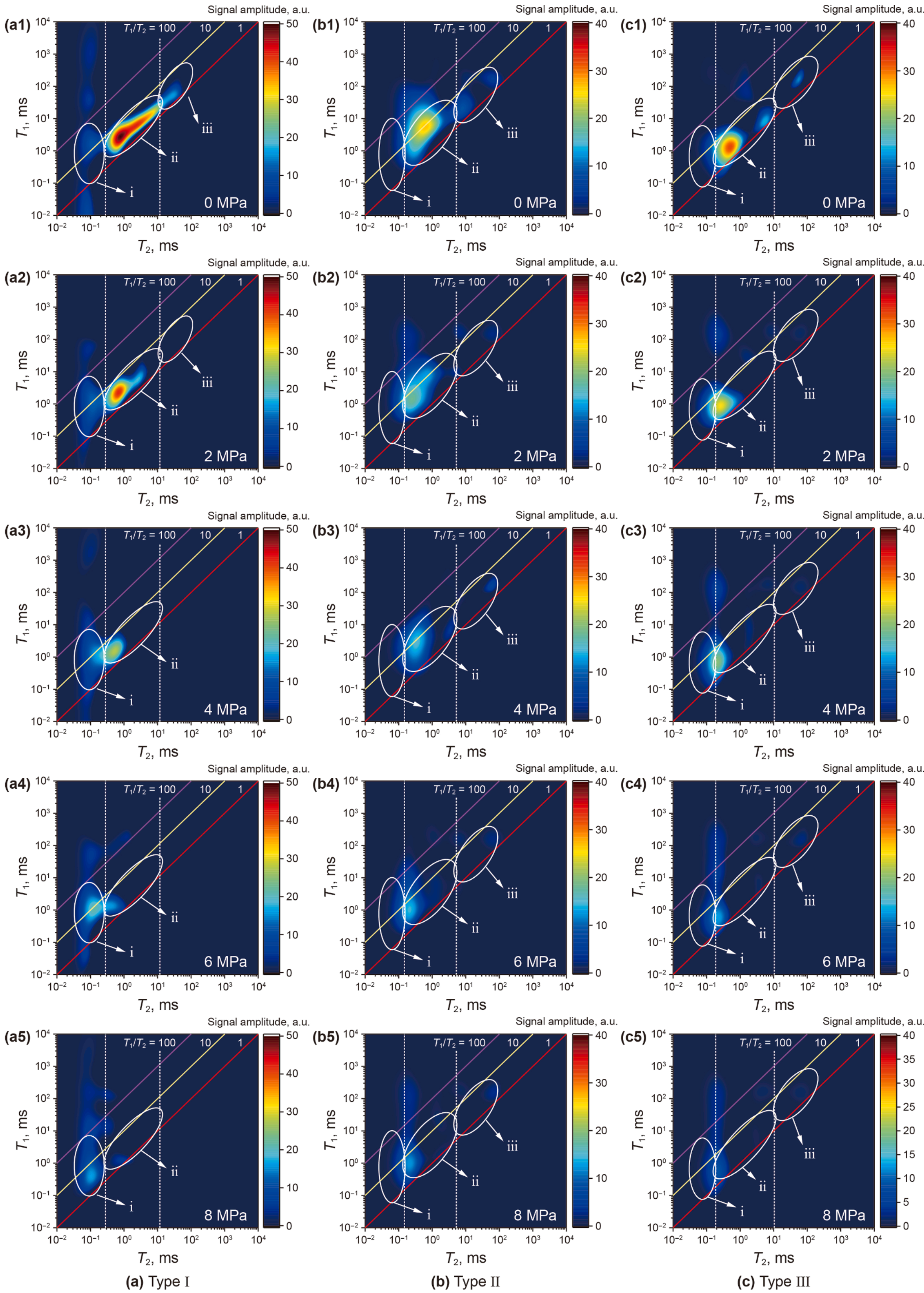

Fig. 15. 2D T_1–T_2 spectra of three types of cores.

flowback pressure increased from 0 to 8 MPa, the signal area in region iii (macropores) gradually decreased, initially rapidly and then more slowly, eventually reaching a minimum retention value of 0. This indicates that free fluids in macropores can be almost completely discharged at a low pressure differential (2 MPa), explaining the rapid mitigation of water blocking damage in macropores. The signal area in region ii (mesopores) decreased by 40%–90%, with an average fracturing fluid retention of 9.79%, indicating that flowback of bound fluids from mesopores is key to alleviating water blocking damage. The signal area in region i (micropores) decreased by less than 50%, with an average retention of 66.24%. Even at 8 MPa, the signal remained prominent, confirming that hydrogen water strongly associated with clay minerals is the primary cause of permanent water blocking in micropores.

4.3. Characteristics of water blocking damage induced by fracturing fluids

4.3.1. Characterization of water blocking damage in different types of cores

To quantitatively characterize the water blocking damage caused by fracturing fluid in cores from different reservoir types, the water blocking degree for pores of various scales was calculated using Eqs. (6) and (7), enabling a quantitative evaluation of water blocking. In the initial phase, the fracturing fluid retention is relatively high, resulting in a substantial overall water blocking degree (Fig. 17). The water blocking degrees for the three core types are 78.08%, 88.74%, and 96.08%, respectively. When the flowback pressure differential reaches 2 MPa, the fracturing fluid retention decreases significantly, with the fluid in macropores being prioritized for recovery. As the flowback pressure differential increases, the amount of fracturing fluid retained in the pores gradually diminishes, thereby reducing the water blocking degree. At 6 MPa, the corresponding water blocking degrees are 29.92%, 31.15%, and 38.02%. With further increase in the flowback pressure differential, both the remaining fracturing fluid and the degree of water blocking damage continue to decrease. When the flowback pressure differential reaches 8 MPa, the reduction in water blocking degree is less than 10%, indicating that the flowback process is nearing completion. At this stage, the water blocking degrees are 21.77%, 24.08%, and 31.87%, respectively.

4.3.2. Characteristics of water blocking damage at different pore scales

As the flowback pressure differential increases, the fracturing fluid in the pores is expelled, reducing the degree of water

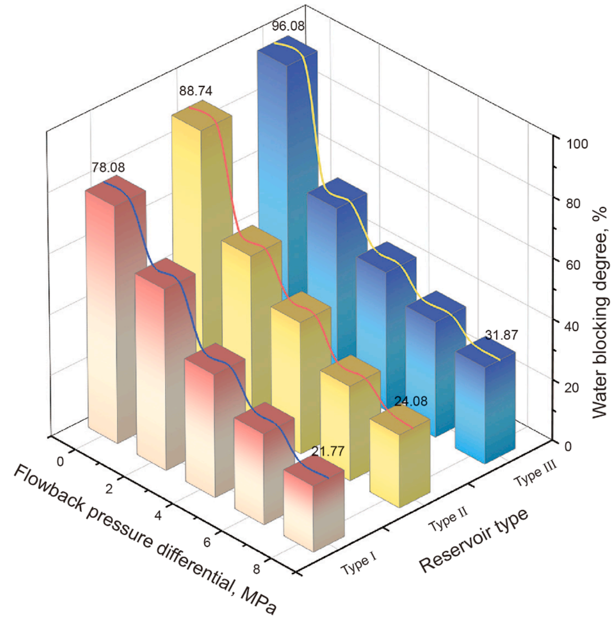

Fig. 17. Degree of water blocking of fracturing fluid in different types of cores.

blocking. For Type I cores (Fig. 18(a)), the total degree of water blocking is lowest at the end of flowback, at 21.77%. During flowback, N_2 tends to migrate along the dominant seepage channels, which results in a limited sweep efficiency of the fracturing fluid. The greatest damage is observed in the micropores. Significant alterations in the fracturing fluid within the pores are observed in Type II cores (Fig. 18(b)), accompanied by the highest degree of water blocking in the micropores, reaching 38.90%. In alignment with the observed patterns in Type I and Type II cores, Type III cores demonstrate increased overall retention of fracturing fluid compared to the other two types (Fig. 18(c)), leading to the greatest degree of water blocking in Type III cores.

In macropores (Fig. 19(a)), the amount of retained fracturing fluid is comparatively low. At a flowback pressure differential of 2 MPa, there is a notable decrease in water blocking degree. At a pressure differential of 8 MPa, the water blocking degree reductions are less than 5%, which reach 13.44%, 25.86%, and 26.40%. With regard to the mesopores (Fig. 19(b)), a notable amount of fracturing fluid is retained. At a pressure differential of 4 MPa, the corresponding water blocking degree are 38.68%, 38.96%, and 36.37%. As the pressure differential increases, the changes in water blocking degree become progressively smaller. In micropores

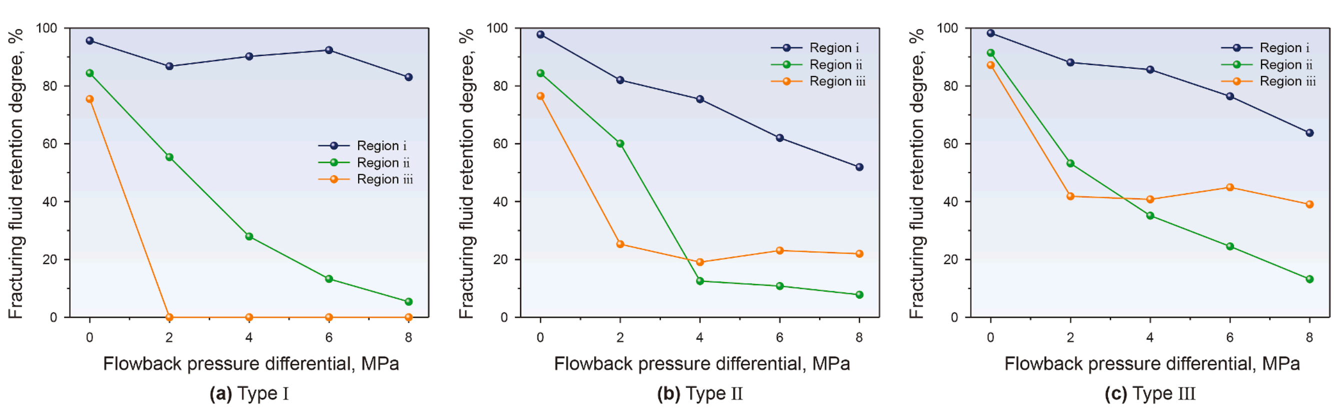

Fig. 16. Fracturing fluid retention degree based on 2D NMR T_1–T_2 spectra.

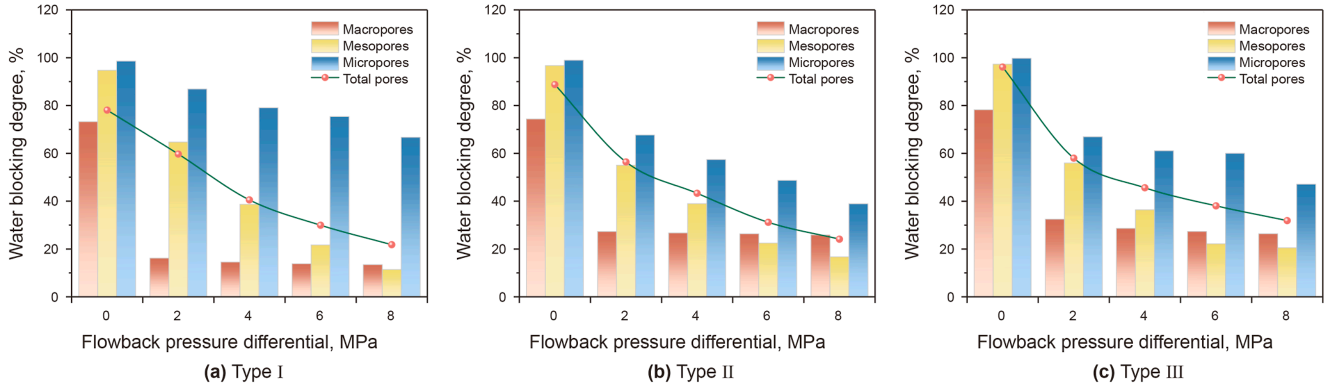

Fig. 18. Degree of water blocking of fracturing fluids at different pore scales in different types of cores.

(Fig. 19(c)), where throat development is limited, the greatest degree of fracturing fluid retention is observed. During flowback, N_2 can readily obstruct the throats, impeding the movement of fracturing fluid within the pores and resulting in significant water blocking. The final degrees of water blocking are 66.74%, 39.90%, and 47.14%, respectively.

The results of the NMR calculations are used to establish a correlation for the water blocking degree of the fracturing fluid across different pore scales. After flowback, the water blocking degree in macropores decreases significantly (Fig. 20(a)), with reductions of 59.79%, 48.52%, and 51.83%. Lower pressure differentials contribute to this reduction in water blocking degree in macropores. The alterations in water blocking degree in mesopores are the most significant (Fig. 20(b)), with reductions of 83.33%, 80.01%, and 76.82%. The fitting curves for Type I and Type III cores demonstrate a superior degree of fit in compared to Type II cores (Fig. 20(c)). The increased capillary forces result in higher water blocking degree in micropores, with reductions of 31.83%, 60.05%, and 52.64%, respectively.

4.4. Mechanism of water blocking damage induced by fracturing fluid

In Type I reservoir cores, the degrees of water blocking in macropores and mesopores decrease significantly with the increase in flowback pressure differential. However, after N_2 breakthrough, gas flows through the main seepage channels, leaving the fracturing fluid in the micropores unswept. The rapid decay of the T_1–T_2 spectral signal in region iii (free fluids) indicates extremely high mobility with negligible confinement effects. The pronounced decrease in signal intensity at low pressure differentials is consistent with weak capillary forces and good connectivity of large pores, demonstrating a strong correspondence between the T_1–T_2 response and the characteristic pore structure.

In Type II reservoir cores, pore connectivity is complex, and effective mobilization of fracturing fluids can reduce water blocking damage. The signal decrease in region ii of the T_1–T_2 spectra reaches 92.20%, corresponding to the lowest water blocking damage observed in mesopores (16.69%), further confirming that medium to high flowback pressure differentials can overcome capillary constraints. Additionally, changes in T_1–T_2 spectral signal values indicate that bound fluid in mesopores constitutes the main fraction of retained fracturing fluid.

In Type III reservoir cores, poor connectivity leads to severe water blocking. This effect leads to a higher degree of water blocking compared to the other two types of reservoir cores, causing severe reservoir damage. The T_1–T_2 spectral signal in region i (hydrogen water) shows negligible decay with increasing flowback pressure differential, and the final water blocking damage reaches 47.14%. The underlying mechanism of water blocking in micropores involves the coupling of strong binding, high capillary pressure, and Jamin effect, which together prevent effective flowback of the fracturing fluid.

In macropores, fracturing fluid retention is minimal and occurs predominantly on the surface of rock particles. As a result, most of the fluid can be recovered, leading to reduced water blocking

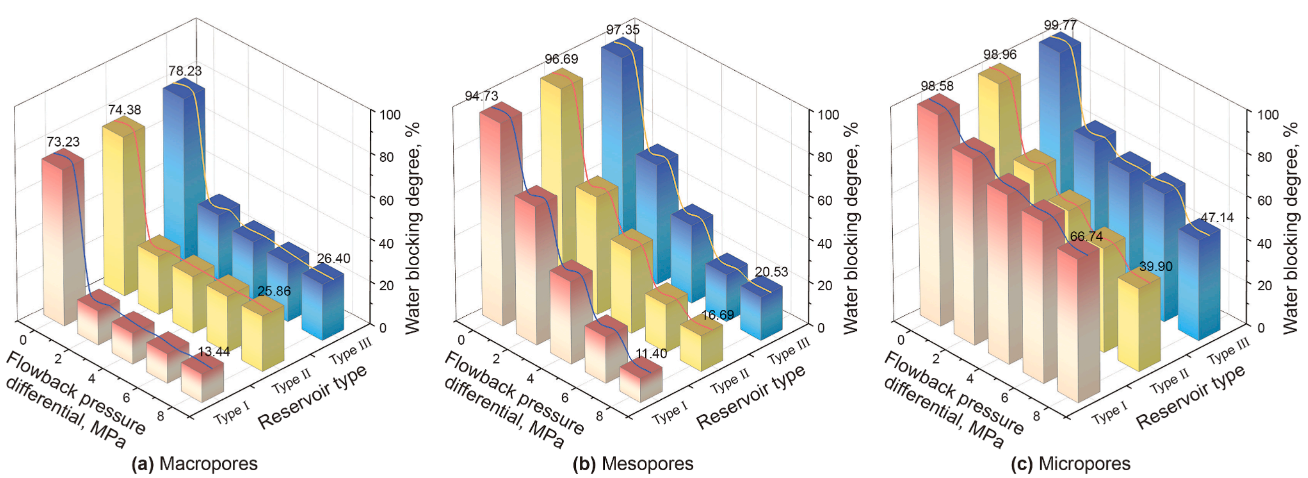

Fig. 19. Degree of water blocking of fracturing fluids at different pore scales.

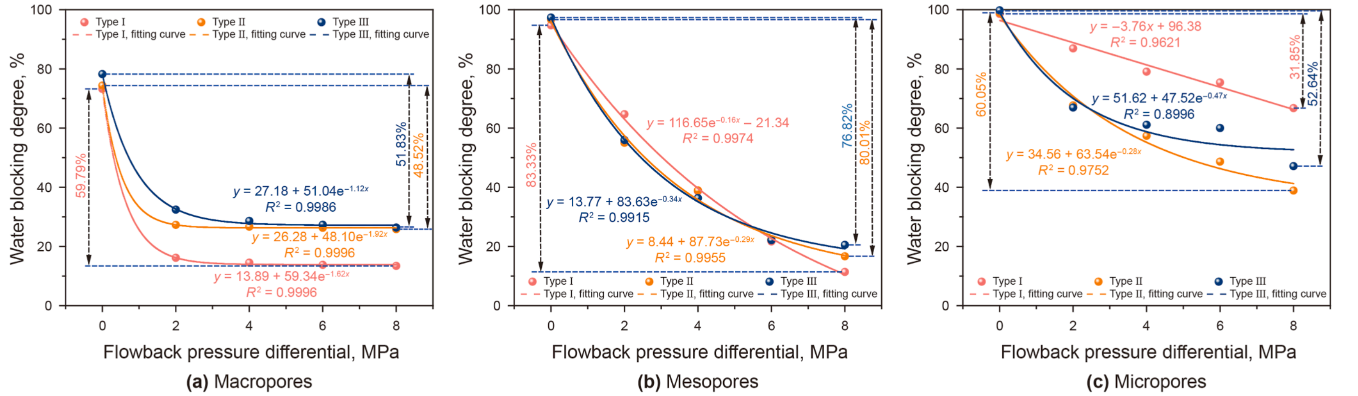

Fig. 20. Correlation of water blocking degree of fracturing fluids at different pore scales.

damage. Conversely, mesopores are the primary regions for fluid retention, exhibiting the highest retention volumes. However, because capillary forces in mesopores are weaker than those in micropores, fluid recovery is still facilitated. In well-developed micropores, reduced pore-throat dimensions enhance capillary forces, making them susceptible to the Jamin effect (Su et al., 2017), which results in the severe water blocking damage (Figs. 21 and 22).

T_2 and T_1–T_2 spectra enable accurate identification of fluid types and signal variation patterns in different pore sizes. As the flowback pressure differential increases, the NMR T_2 spectra shift leftward, the curve amplitude decreases, and the T_1–T_2 spectra signals in various regions diminish. Consequently, while the degrees of water blocking damage are reduced in mesopores and macropores, the retention in micropores remains unchanged. This persistent retention ultimately results in long-term or even permanent water blocking damage in micropores.

Due to differences in fluid phases, the flowback in tight gas reservoir involves a gas–water two-phase flow of natural gas (mainly methane) and fracturing fluid, whereas this experiment used N_2 as a surrogate. The physical properties of N_2 differ from those of methane, which may slightly reduce its gas-drive efficiency and cause some quantitative deviation from actual field conditions. However, the experimental results demonstrate that increasing the flowback pressure differential reduces the degree of water blocking damage, and micropores and mesopores remain the primary retention spaces for fracturing fluids. The reliability of these core trends is not affected.

This study focused on the Shan 1 member in the Sulige gas field of the Ordos Basin, with limitations including a restricted range of core types and sample numbers, a single experimental temperature, and the lack of consideration of coupled chemical damage. To address these limitations and enhance the reference value of the research, future work will focus on: (1) conducting comparative experiments to establish a generalized evaluation method for water blocking damage that accounts for lithological and regional differences; (2) developing a temperature-coupled quantitative model to predict water blocking damage; and (3) constructing a comprehensive evaluation system that integrates both physical water blocking and chemical damage mechanisms.

Based on the water blocking damage mechanisms revealed by NMR T_2 and T_1–T_2 spectra, this study provides practical insights for the development of tight gas reservoirs across three key dimensions: optimization of fracturing design, control of flowback parameters, and assessment of reservoir risk. To further validate the applicability of the proposed pore-scale water blocking patterns and flowback parameters, subsequent field tests are recommended based on reservoir type classification. These tests

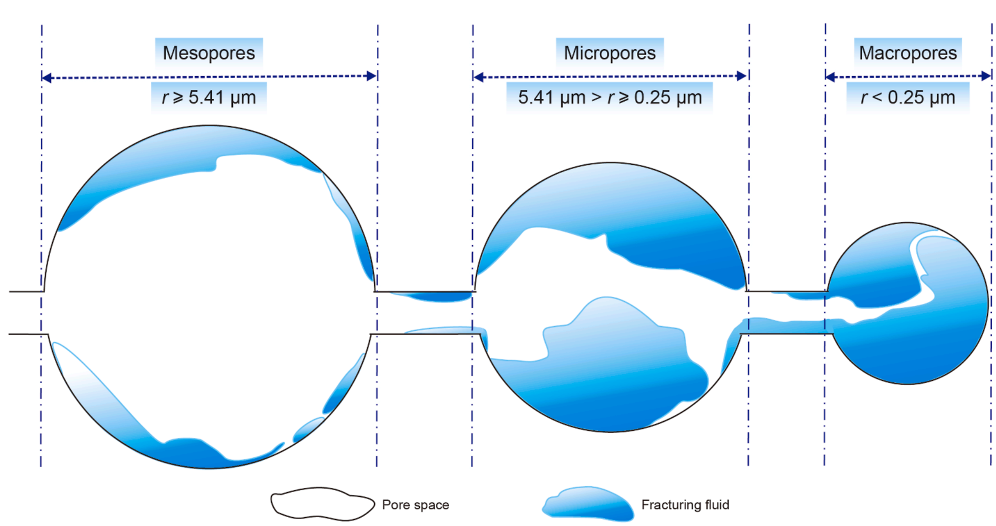

Fig. 21. Retention characteristics of fracturing fluids at different pore scales.

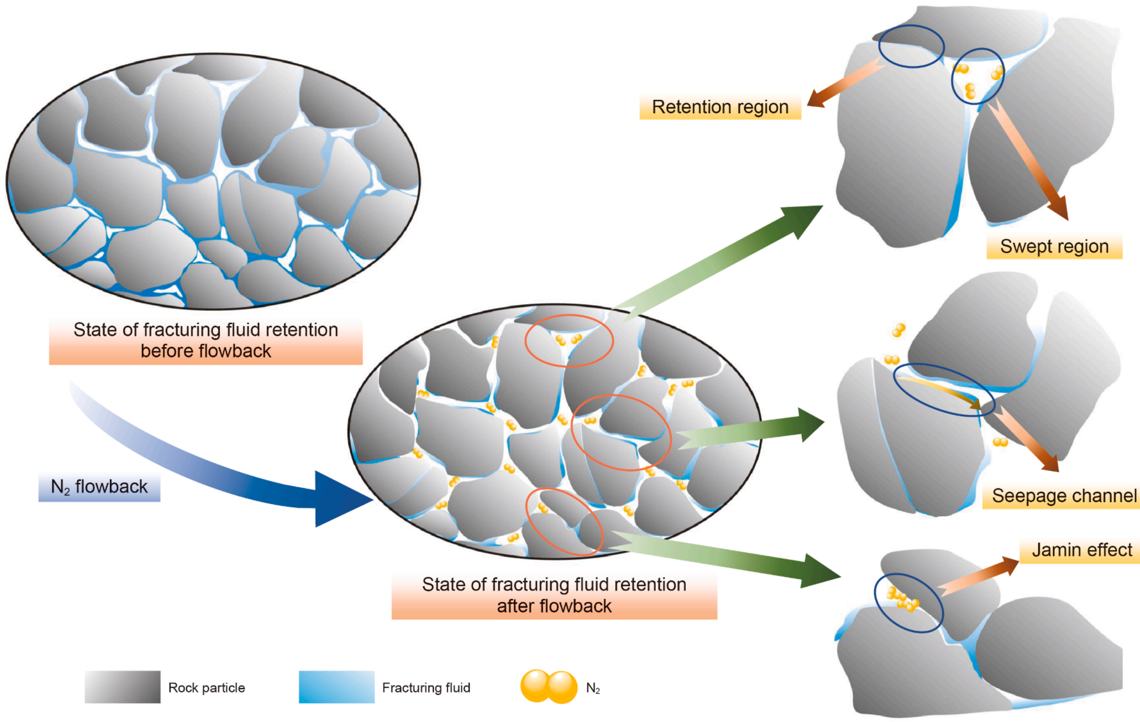

Fig. 22. Mechanism diagram of water blocking damage induced by fracturing fluids.

should monitor both the water content in flowback fluid and gas production rates under different schemes, thereby enabling the gradual refinement of the field testing methodologies.

5. Conclusions

Using one-dimensional NMR T_2 spectra and two-dimensional NMR T_1–T_2 spectra, a distribution map of hydrogen-containing substances in tight gas reservoirs was constructed. This study aimed to analyze the retention characteristics of fracturing fluids, characterize the degree ofwater blocking damage induced by fracturing fluid, investigate the influence of flowback pressure differential on the retention and degree of water blocking at different pore scales, and elucidate the mechanism of water blocking damage induced by fracturing fluid. The primary conclusions of this investigation are as follows:

(1) NMR T_2 spectra reveals that the fracturing fluids primarily occupy the micropores and mesopores. As the flowback pressure differential increases, the water blocking damage significantly decreases across various reservoir types, with Type I reservoir cores exhibiting lower water blocking damage than Type II and Type III cores.
(2) A distribution map of the hydrogen-containing substances in tight gas reservoirs was established based on the types of substances present in the cores and by combining NMR T_2 and T_1–T_2 techniques. The hydrogen-containing substances in the cores can be classified into three regions: hydrogen water, bound fluid, and free fluid.
(3) Utilizing T_1–T_2 NMR technology, the degree of pore development and the retention of fracturing fluids can be observed visually in the resulting T_1–T_2 spectra. As the flowback pressure differential increases, there is a notable change in signal values within the bound water region, indicating a reduction in fracturing fluid retention and a decrease in water blocking damage.
(4) The pore classification results indicate that the degree of water blocking is minimal in macropores, while that in both mesopores and micropores exceed 90%. After flowback, the alteration in water blocking degree is most evident in mesopores, with micropores exhibiting the highest degree of water blocking, which may result in long-term or permanent damage.

CRediT authorship contribution statement

Xiao-Hang Li: Writing – original draft, Conceptualization. **Hui Gao:** Writing – review & editing, Methodology. **Yong-Gang Xie:** Funding acquisition. **Hua-Qiang Shi:** Funding acquisition, Supervision. **Hua-Zhou Li:** Formal analysis, Investigation. **Teng Li:** Formal analysis. **Zhi-Lin Cheng:** Project administration. **Chen Wang:** Investigation. **Kai-Qing Luo:** Data curation.

Declaration of competing interest

The authors declare that they have no known competing financial interests or personal relationships that could have appeared to influence the work reported in this paper.

Acknowledgments

The authors would like to acknowledge the support of the National Natural Science Foundation of China (Grant Nos. 52174030 and 52474042), the Natural Science Basic Research Program of Shaanxi (Program No. 2025JC-JCQN-013), the Natural

Science Basic Research Plan in Shaanxi Province of China (Program No. 2024JC-YBMS-256), the Postgraduate Innovation Fund Project of Xi'an Shiyou University (Program No. YCX2611002), and the Open Fund of National Key Laboratory of Oil and Gas Reservoir Geology and Exploitation (Southwest Petroleum University) (Grant No. PLN2023-21).

References

Almubarak, T., Ng, J.H.C., AlKhaldi, M., et al., 2020. Insights on potential formation damage mechanisms associated with the use of gel breakers in hydraulic fracturing. Polymers 12 (11), 2722. https://doi.org/10.3390/polym12112722.

Bahrami, N., Soroush, S., Hossain, M., et al., 2015. Evaluation of damage mechanisms in tight gas reservoirs: Field example from Perth Basin. In: SPE Kingdom of Saudi Arabia Annual Technical Symposium and Exhibition. https://doi.org/10.2118/178018-MS.

Dai, C.L., Cheng, R., Sun, X., et al., 2019. Oil migration in nanometer to micrometer sized pores of tight oil sandstone during dynamic surfactant imbibition with online NMR. Fuel 245, 544–553. https://doi.org/10.1016/j.fuel.2019.01.021.

Fu, L.P., Liao, K.L., Ge, J.J., et al., 2020. Study on the damage and control method of fracturing fluid to tight reservoir matrix. J. Nat. Gas Sci. Eng. 82, 103464. https://doi.org/10.1016/j.jngse.2020.103464.

Gao, H., Li, H.Z., 2015. Determination of movable fluid percentage and movable fluid porosity in ultra-low permeability sandstone using nuclear magnetic resonance (NMR) technique. J. Pet. Sci. Eng. 133, 258–267. https://doi.org/10.1016/j.petrol.2015.06.017.

Gao, H., Liu, Y.L., Zhang, Z., et al., 2015. Impact of secondary and tertiary floods on microscopic residual oil distribution in medium-to-high permeability cores with NMR technique. Energy Fuels 29 (8), 4721–4729. https://doi.org/10.1021/acs.energyfuels.5b00394.

Gao, H., Wang, C., Cheng, Z.L., et al., 2023. Effect of pressure pulse stimulation on imbibition displacement within a tight sandstone reservoir with local variations in porosity. Geoenergy Sci. Eng. 226, 211811. https://doi.org/10.1016/j.geoen.2023.211811.

Gao, H., Li, X.H., Li, T., et al., 2024. Characteristics of oil production by fracturing fluid additive-assisted displacement in tight oil reservoirs. Energy Fuels 38 (18), 17541–17553. https://doi.org/10.1021/acs.energyfuels.4c02634.

Gu, M.X., Xie, R.H., Guo, J.F., et al., 2023. Evaluation of fluid saturation in shale using 2D nuclear magnetic resonance. Energy Fuels 37 (4), 2713–2720. https://doi.org/10.1021/acs.energyfuels.2c03383.

Guo, Q., Lu, X.J., Liu, T., et al., 2024. Pore structure characterization and its influence on aqueous phase trapping damage in tight gas sandstone reservoirs. PLoS One 19 (4), 27. https://doi.org/10.1371/journal.pone.0298672.

Guo, T.L., Xiong, L., Ye, S.J., et al., 2023. Theory and practice of unconventional gas exploration in carrier beds: Insight from the breakthrough of new type of shale gas and tight gas in Sichuan Basin, SW China. Petrol. Explor. Dev. 50 (1), 27–42. https://doi.org/10.1016/S1876-3804(22)60367-7.

He, J.W., Li, H., Lu, J.X., et al., 2024. Variations in the pore structure and fluid mobility under anionic surfactant assisted matrix acidification of coal based on nuclear magnetic resonance T_1-T_2 spectra. Fuel 355, 129488. https://doi.org/10.1016/j.fuel.2023.129488.

He, Y.W., Shang, Y.Z., Wu, W.S., et al., 2024. Investigating recovery potential through depletion development of tight oil reservoirs via NMR technology. Energy Fuels 38 (1), 333–340. https://doi.org/10.1021/acs.energyfuels.3c03947.

Hu, S.Y., Zhu, R.K., Wu, S.T., et al., 2018. Exploration and development of continental tight oil in China. Petrol. Explor. Dev. 45 (4), 790–802. https://doi.org/10.1016/S1876-3804(18)30082-X.

Huang, H., Babadagli, T., Chen, X., et al., 2020. Performance comparison of novel chemical agents for mitigating water-blocking problem in tight gas sandstones. SPE Reservoir Eval. Eng. 23 (4), 1150–1158. https://doi.org/10.2118/199282-PA.

Li, B., Yin, G.F., Wang, A.L., et al., 2025. New method for nuclear magnetic resonance dual echo time logging interpretation and fluid identification in tight sandstone gas reservoirs. SPE J. 30 (4), 1906–1921. https://doi.org/10.2118/224432-PA.

Li, C.L., Tan, M.J., Wang, K.W., et al., 2022. Comparison of different inversion methods of D-T_2 two-dimensional nuclear magnetic resonance logging and applicability analysis. Appl. Geophys. 19 (2), 173–184. https://doi.org/10.1007/s11770-022-0983-x.

Li, H., Guo, Q.Y., Liu, M., et al., 2024. Petrophysical characterization of coal subjected to cyclic *N*-methylpyrrolidone treatment based on two-dimensional NMR T_1-T_2. Fuel 365, 131189. https://doi.org/10.1016/j.fuel.2024.131189.

Li, T., Gao, H., Wang, C., et al., 2022. Oil utilization degree at various pore sizes via different displacement methods. J. Pet. Explor. Prod. Technol. 12 (8), 2271–2287. https://doi.org/10.1007/s13202-022-01464-7.

Li, Y., Guo, J.C., Wang, S.B., 2019. The damage mechanisms of fracturing fluid on production in tight gas reservoirs. Energy Proc. 158, 5988–5993. https://doi.org/10.1016/j.egypro.2019.01.521.

Li, Y.Z., Jiang, G.C., Li, X.Q., et al., 2022. Quantitative investigation of water sensitivity and water locking damages on a low-permeability reservoir using the core flooding experiment and NMR test. ACS Omega 7 (5), 4444–4456. https://doi.org/10.1021/acsomega.1c06293.

Liu, H.X., Gao, S.S., Fang, F.F., et al., 2023. Model of cross-flow interference index and application for multi-layer commingled production in Sulige tight sandstone gas reservoir, Ordos Basin, China. J. Nat. Gas Geosci. 8 (6), 389–401. https://doi.org/10.1016/j.jnggs.2023.09.003.

Ma, X.H., 2021. "Extreme utilization" development theory of unconventional natural gas. Petrol. Explor. Dev. 48 (2), 381–394. https://doi.org/10.11698/PED.2021.02.09.

Montrazi, E.T., Lucas-Oliveira, E., Araujo-Ferreira, A.G., et al., 2018. Simultaneous acquisition for T_2–T_2 exchange and T_1–T_2 correlation NMR experiments. J. Magn. Reson. 289, 63–71. https://doi.org/10.1016/j.jmr.2018.02.008.

Naik, S., Yang, S., Woolley, M., et al., 2019. Analytical modelling of the water block phenomenon in hydraulically fractured wells. J. Nat. Gas Sci. Eng. 67, 56–70. https://doi.org/10.1016/j.jngse.2019.04.018.

Ramalingam, K., Balasubramanian, D., Chellakumar, P.J.T.J.S., et al., 2020. An assessment on production and engine characterization of a novel environment-friendly fuel. Fuel 279, 118558. https://doi.org/10.1016/j.fuel.2020.118558.

Silletta, E.V., Vila, G.S., Domené, E.A., et al., 2022. Organic matter detection in shale reservoirs using a novel pulse sequence for T_1-T_2 relaxation maps at 2 MHz. Fuel 312, 122863. https://doi.org/10.1016/j.fuel.2021.122863.

Singer, P.M., Chen, Z.L., Wang, X.L., et al., 2020. Diffusive coupling in heptane-saturated kerogen isolates evidenced by NMR T_1-T_2 and T_2-T_2 maps. Fuel 280, 118626. https://doi.org/10.1016/j.fuel.2020.118626.

Song, Z.Z., Lv, M.Y., Zhao, L.B., et al., 2024. A novel bound water occurrence model for tight sandstone. Fuel 357, 130030. https://doi.org/10.1016/j.fuel.2023.130030.

Su, X.B., Wang, Q., Song, J.X., et al., 2017. Experimental study of water blocking damage on coal. J. Pet. Sci. Eng. 156, 654–661. https://doi.org/10.1016/j.petrol.2017.06.048.

Sun, L.D., Zou, C.N., Jia, A.L., et al., 2019. Development characteristics and orientation of tight oil and gas in China. Petrol. Explor. Dev. 46 (6), 1073–1087. https://doi.org/10.1016/S1876-3804(19)60264-8.

Sun, M.D., Zhang, L.H., Hu, Q.H., et al., 2019. Pore connectivity and water accessibility in Upper Permian transitional shales, southern China. Mar. Petrol. Geol. 107, 407–422. https://doi.org/10.1016/j.marpetgeo.2019.05.035.

Tang, H.M., Tang, H.X., He, J., et al., 2021. Damage mechanism of water-based fracturing fluid to tight sandstone gas reservoirs: Improvement of *The Evaluation Measurement for Properties of Water-based Fracturing Fluid: SY/T 5107-2016*. Nat. Gas. Ind. B 8 (2), 163–172. https://doi.org/10.1016/j.ngib.2020.09.016.

Wang, J., Zhou, F.J., 2021. Cause analysis and solutions of water blocking damage in cracked/non-cracked tight sandstone gas reservoirs. Pet. Sci. 18 (1), 219–233. https://doi.org/10.1007/s12182-020-00482-6.

Wang, J., Huang, Y.X., Zhang, Y., et al., 2020a. Study of fracturing fluid on gel breaking performance and damage to fracture conductivity. J. Pet. Sci. Eng. 193, 107443. https://doi.org/10.1016/j.petrol.2020.107443.

Wang, J., Li, Y.F., Zhou, F.J., et al., 2020b. Study on the mechanism of nanoemulsion removal of water locking damage and compatibility of working fluids in tight sandstone reservoirs. ACS Omega 5 (6), 2910–2919. https://doi.org/10.1021/acsomega.9b03744.

Wang, X.Z., Qiao, X.Y., Mi, N.Z., et al., 2019. Technologies for the benefit development of low-permeability tight sandstone gas reservoirs in the Yan'an gas field, Ordos Basin. Nat. Gas. Ind. B 6 (3), 272–281. https://doi.org/10.1016/j.ngib.2018.11.017.

Wang, Y., Chang, X.C., Liu, Z.Y., et al., 2023. Occurrence state and oil content evaluation of Permian Fengcheng Formation in the Hashan area as constrained by NMR and multistage Rock-Eval. Pet. Sci. 20 (3), 1363–1378. https://doi.org/10.1016/j.petsci.2022.11.019.

Wu, B.H., Xie, R.H., Wang, X.Y., et al., 2020. Characterization of pore structure of tight sandstone reservoirs based on fractal analysis of NMR echo data. J. Nat. Gas Sci. Eng., 103483 https://doi.org/10.1016/j.jngse.2020.103483.

Xu, J.G., Qiu, Z.S., Zhao, X., et al., 2019. Study of 1-octyl-3-methylimidazolium bromide for inhibiting shale hydration and dispersion. J. Pet. Sci. Eng. 177, 208–214. https://doi.org/10.1016/j.petrol.2019.02.064.

Zhao, F.L., Liu, P.C., Hao, S.Y., et al., 2021. A new dynamic capillary-number-recovery evaluation method for tight gas reservoirs. J. Pet. Sci. Eng. 204, 108730. https://doi.org/10.1016/j.petrol.2021.108730.

Zhao, X., Wang, G.Q., Zhang, Y.G., et al., 2023. Application of digital rock technology for formation damage evaluation in tight sandstone reservoir. J. Pet. Explor. Prod. Technol. 13 (3), 803–812. https://doi.org/10.1007/s13202-022-01576-0.

Zhang, P.F., Lu, S.F., Li, J.Q., et al., 2023. Quantitative characterization of shale pore connectivity and controlling factors using spontaneous imbibition combined with nuclear magnetic resonance T_2 and T_1-T_2. Pet. Sci. 20 (4), 1947–1960. https://doi.org/10.1016/j.petsci.2023.03.011.

Zhang, X.P., Liu, Y.Y., Liu, Y.Z., et al., 2022. Influencing factors and application of spontaneous imbibition of fracturing fluids in tight sandstone gas reservoir. ACS Omega 7 (43), 38912–38922. https://doi.org/10.1021/acsomega.2c04648.

Zhang, X.P., Liu, Y.Q., Zhou, L., et al., 2023. Study on matrix damage and control methods of fracturing fluid on tight sandstone gas reservoirs. ACS Omega 8 (40), 37461–37470. https://doi.org/10.1021/acsomega.3c05461.

Zhang, Y.Y., Jiang, S., He, Z.L., et al., 2022. Characteristics of heterogeneous diagenesis and modification to physical properties of upper Paleozoic tight gas reservoir in eastern Ordos Basin. J. Pet. Sci. Eng. 208, 109243. https://doi.org/10.1016/j.petrol.2021.109243.

Zhou, J.S., Qiao, X.Y., Wang, R.G., et al., 2022. Effective reservoir development model of tight sandstone gas in Shanxi Formation of Yan'an gas field, Ordos Basin, China. J. Nat. Gas Geosci. 7 (2), 73–84. https://doi.org/10.1016/j.jnggs.2022.04.003.

Zou, C.N., Zhai, G.M., Zhang, G.Y., et al., 2015. Formation, distribution, potential and prediction of global conventional and unconventional hydrocarbon resources. Petrol. Explor. Dev. 42 (1), 14–28. https://doi.org/10.1016/S1876-3804(15)60002-7.

Zou, C.N., Yang, Z., He, D.B., et al., 2018. Theory, technology and prospects of conventional and unconventional natural gas. Petrol. Explor. Dev. 45 (4), 604–618. https://doi.org/10.1016/S1876-3804(18)30066-1.